Engineering Analysis with Boundary Elements 45 (2014) 29–35

Contents lists available at ScienceDirect

Engineering Analysis with Boundary Elements

journal homepage: www.elsevier.com/locate/enganabound

3D Lattice Boltzmann flow simulations through dendritic mushy zones

A. Ludwig [a,b,*], A. Kharicha [a,b], C. Hölzl [c], J. Domitner [b], M. Wu [a], T. Pusztai [d]

[a] Department of Metallurgy, Chair of Simulation and Modeling of Metallurgical Processes, University of Leoben, 8700 Leoben, Austria
[b] Christian Doppler Laboratory for Multiphase Simulation of Metallurgical Processes, 8700 Leoben, Austria
[c] Material Center Leoben, 8700 Leoben, Austria
[d] Reasearch Institute for Solid State Physics and Optics, 1121 Budapest, Hungary

ARTICLE INFO

Article history:
Received 9 February 2012
Accepted 25 May 2013
Available online 21 February 2014

Keywords:
Lattice-Boltzmann method
Alloy solidification
Mush permeability
Dendritic microstructure

ABSTRACT

Literature data on permeability of dendritic microstructures show a wide scatter. For a given solid fraction the permeability may vary easily by two orders of magnitude. This might be caused by some unavoidable technical problems in doing the corresponding experiments. However, even numerical results may vary greatly depending on the source of the input microstructure and/or the dimension of flow simulation (2D vs. 3D) and/or the applied boundary conditions. In the present work we have used the Lattice Boltzmann technique to perform flow simulations through 2D and 3D dendritic microstructures coming from (i) simplified geometrical approximations, (ii) phase field simulations of binary alloys and (iii) computer tomographs on AlCu alloys. The discussion of the results shows that for low solid fraction, simple geometries can be used as substitute for dendritic structures. However, once the secondary arms are more prominent, large deviations and scattering occur. These deviations are caused by the strong variation of the dendrites geometry along the growth direction, making simplified structures insufficient to derive a reasonable value for the permeability.

1. Introduction

The vast majority of metallic alloys solidify by forming a dendritic mushy zone. Depending on the local solid fraction such a dendritic mushy zone acts like a more or less permeable media for any melt flow which may occur during solidification. Since the alloy elements are differently segregated in the interdendritic melt, flow through these areas often lead to the occurrence of macrosegregation, a phenomenon which tremendously deteriorate the quality of large castings or of continuously cast strands or billets. In order to find ways to reduce such macrosegregation, corresponding numerical solidification models need to have reliable permeability data for the dendritic mushy zone.

In 1974, Apelian et al. showed for two aluminum alloys that porous media theory might be valid for describing the flow through a dendritic network [1]. When distilled water was forced through dendritic structures from which liquid had been removed, it was found that Darcy's law [2] was followed. When inertial effects are negligible, Darcy's law is written as

$$g_\ell \vec{v} = -\frac{\overline{\overline{K}}}{\mu_\ell}\nabla p, \tag{1}$$

where $\vec{v}$ is the velocity of the interdendritic liquid, μ_ℓ is its dynamic viscosity, g_ℓ is the volume fraction of interdendritic liquid, $\overline{\overline{K}}$ is the second-rank permeability tensor and p is the pressure. The product $g_\ell \vec{v}$ is also called superficial velocity. The main difference between an equiaxed and a columnar dendritic array is that the permeability of an equiaxed dendritic structure is almost isotropic, whereas for a columnar dendritic structure it depends on whether the flow is parallel or normal to the primary dendrite arms. Thus, for equiaxed dendrites $\overline{\overline{K}}$ is effectively scalar (i.e., $\overline{\overline{K}} = K\overline{\overline{I}}$), whereas in columnar systems, $\overline{\overline{K}}$ is treated as diagonal with two unique values: K_{zz} parallel to the principal growth direction and $K_{xx} = K_{yy}$ for flow transverse to the dendrites. Therefore research on permeability in mushy zones can naturally be divided between investigations of equiaxed and columnar structures. An extended overview on experimental investigations on permeabilities of dendritic structures can be found in [1,3–16].

In order to discuss the observed permeability difference between grain-refined and nongrain-refined specimens, the specific surface area, $S_V := A_\ell / V_0$, with A_ℓ being the surface area of liquid–solid interface, and V_0 the corresponding two-phase

* Corresponding author at: University of Leoben, Department of Metallurgy, Chair of Simulation and Modeling of Metallurgical-Metallurgical Processes, 8700 Leoben, Austria.
E-mail address: ludwig@unileoben.ac.at (A. Ludwig).

http://dx.doi.org/10.1016/j.enganabound.2014.01.015
0955-7997

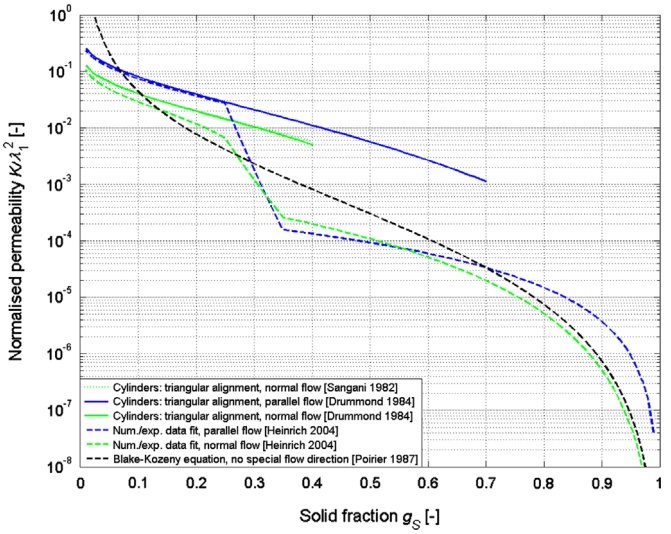

Fig. 1. Normalized permeability of dendritic mushy zones as function of solid volume fraction taken from different literature sources. (For interpretation of the references to color in this figure caption, the reader is referred to the web version of this paper.)

volume, was introduced as additional parameter. In the following works the reciprocal of the specific surface area S_V^{-1} was recognized as a relevant length scale for permeability [5,7,8,10,12,17,18]. Although S_V^{-1} is a natural length-scale, it is difficult to directly measure during practical solidification, this is why researchers estimated it from the length of the primary or the secondary dendrite arm spacing λ_1 [3].

For high liquid fractions (i.e. $g_\ell > 0.65$), it was found difficult to obtain experimental data for permeability because the dendrites do not remain coherent during testing [7,12,17]. Consequently, researchers have used numerical simulations of the interdendritic flow to estimate mushy zone permeability for high liquid fractions [5,8,11,13,14,18–20]. Heinrich et al. did a synthesis of empirical and numerical data for the columnar case [21]. They found that in opposite for an equiaxed dendritic microstructure, the permeability correlations for columnar dendritic structures reveal three distinct regions for the flow in both transverse and parallel direction to the dendrite axis. The corresponding data fits are shown in Fig. 1. Heinrich and Poirier describe the occurrence of these three regions by using empirical data for low liquid fractions and results from numerical simulations for higher liquid fractions [21]. For the intermediate region ($0.65 < g_\ell < 0.75$) a simple interpolation between the endpoints of the two data sets was used. The fact that the low-g_ℓ (predominantly experimental) and high-g_ℓ numerical simulations do not merge is not understood. Ganesan et al. [5] and Heinrich and Poirier [21] state that the underlying flow morphology changes from one resembling flow through parallel or transverse cylinders, to one resembling flow through constricting tubes. This change must be continuous, and so it does not explain the step change between permeability at low and high g_ℓ. Possible origin of the discrepancy could lie in the use of a badly estimated λ_1 (vice S_V^{-1}) as the length-scale for dimensionalized K, or in the orientation of channel structures in high g_ℓ giving rise to a non-diagonal $\overline{\overline{K}}$ in the coordinate system used (i.e., perpendicular and parallel to the direction of primary-arm growth).

Beside the best fits on numerical and experimental permeability data published in [21], Fig. 1 shows also the analytical solutions from [22,23] as well as the widely used Black-Kozeny equation adapted for dendritic structure [3,24]. Sangani et al. and Drummond et al. analyzed the drag forces for Stokes flow through two-dimensional (2D) periodic square, rectangular, triangular and hexagonal arrays of circular cylinders parallel and perpendicular to the cylinder axes. Obviously, these analytical solutions superpose for low solid fractions with permeability curves suggested by [21,24]. However, the widely used Blake-Kozeny permeability equations [3] is far off the other curves.

According to the studies mentioned above, it appears that macroscopic modeling could definitely be improved by explicitly considering the liquid fraction gradients in the macroscopic momentum equation and by taking into account the microstructure (tortuosity) of the mushy zone. The dendritic columnar region is characterized by a strong anisotropy [3,25,26] and by the non-uniform macroscopic properties such as the liquid volume fraction, which continuously changes from unity in the melt to zero in the solid region. Although these continuous variations can obviously lead to important differences in the convective flows [27], they have rarely been explicitly taken into account in the theoretical models.

In the present paper, we have performed Lattice Boltzmann flow simulations through dendritic mushy zone whereby the 2D and 3D dendritic microstructures used as input came from three different sources, (i) predefined 2D artificial morphologies, (ii) phase field dendrites, and (iii) computer-tomographs taken from an Al–Cu alloy with about 35 vol.% numerically removed interdendritic eutectic. In the following, the numerical procedure is described. Then, results on flow simulations through the three different input microstructures are presented and discussed. Finally, conclusions were drawn.

2. Numerical procedure

To investigate the interdendritic fluid flow passing through the dendritic structure, the open source library *Palabos* was utilized [28], which provides a modular $C++$ written code based on the Lattice Boltzmann (LB) method [29–33]. This method is advantageous for solving fluid flow problems in complex shaped structures containing irregular boundaries within reasonable calculation time. Generally, Lattice Boltzmann (LB) methods can be regarded as discretized modifications of the Boltzmann equation. By simulating streaming and collision processes across a limited number of fictive particles, the intrinsic particle interactions show viscous flow behavior applicable across the greater mass. With collision models such as the widely used one of Bhatnagar–Gross–Krook [34], the solution of the discretized Boltzmann equation is known to produce similar results than the classical Navier–Stokes-equation. In order to describe the propagation and collision of the fictitious particles in a computer algorithm, the collision and the streaming step are defined as follows:

$$\text{Collision step} \quad f_i(\vec{x}, t+\Delta t) = f_i(\vec{x}, t) + \frac{1}{\tau}(f_i^{eq}(\vec{x}, t) - f(\vec{x}, t)) + \Delta t \cdot F_i, \tag{2}$$

$$\text{Streaming step} \quad f_i(\vec{x} + \vec{c}_i \Delta t, t+\Delta t) = f_i(\vec{x}, t+\Delta t), \tag{3}$$

with $f_i(\vec{x}, t)$ being the distribution function of the particle populations along the directions i at the spatial position $\vec{x}$ and time t. $\vec{c}_i$ is the microscopic velocity vector, Δt the discrete time step and F_i the body force component. τ stands for the dimensionless relaxation time of the fluid. The number of possible propagation directions i in the rectangular lattice depends on the chosen LB model. For the simulations presented here, a three-dimensional model (D3) considering 19 directions (Q19) was applied. Therefore, $i=0, 1, 2, \ldots, 18$ in this D3Q19 model. The equilibrium distribution function of the populations is given by

$$f_i^{eq}(\vec{x}, t) = w_i \rho \left(1 + 3\vec{c}_i \cdot \vec{u} + \frac{9}{2}(\vec{c}_i \cdot \vec{u})^2 - \frac{3}{2}\vec{u} \cdot \vec{u}\right), \tag{4}$$

where the weighting factors in this collision operator, w_i, depend on the chosen LB model. According to [29], we have used $w_0 = 1/3$, $w_{1-6} = 1/18$ and $w_{7-18} = 1/36$ for the D3Q19 model. The macroscopic fluid density, ρ, and the macroscopic fluid velocity, $\vec{u}$, are given by

$$\rho = \sum_{i=0}^{18} f_i \text{ and } \rho\vec{u} = \sum_{i=0}^{18} f_i \vec{c}_i. \tag{5}$$

Note that this single relaxation LB method considers a dimensionless system. In order to converge to the full Navier–Stokes equation with dimensions, we consider the mass and momentum conservation equations in the physical system indexed with p:

$$\nabla_p u_p = 0, \tag{6}$$

$$\frac{\partial u_p}{\partial t_p} + u_p \nabla_p u_p = -\frac{1}{\rho_p}\nabla_p p_p + \nu_p \nabla_p{}^2 u_p. \tag{7}$$

Here, ρ_p is the physical density and ν_p the physical viscosity. With the reference length, $l_{ref,p}$, and the reference time, $t_{ref,p}$, and by used for the following dimensionless quantities indexed with d

$$t_d = \frac{t_p}{t_{ref,p}},\ l_d = \frac{l_p}{l_{ref,p}},\ u_d = \frac{t_{ref,p}}{l_{ref,p}} u_p \text{ and } p_d = \frac{t^2_{ref,p}}{\rho_p l^2_{ref,p}} p_p. \tag{8}$$

Eqs. (6) and (7) are made dimensionless. Hence, we obtain the dimensionless version of Eq. (7):

$$\frac{\partial u_d}{\partial t_d} + u_d \nabla_d u_d = -\nabla_d p_d + \frac{1}{\mathrm{Re}} \nabla_d{}^2 u_d. \tag{9}$$

where the Reynolds Number, Re, is defined as

$$\mathrm{Re} = \frac{l^2_{ref,p}}{\nu_p t_{ref,p}}. \tag{10}$$

Comparing Eqs. (7) and (9) shows that the following conditions holds

$$\nu_d = \frac{1}{\mathrm{Re}} \text{ and } \rho_d = 1. \tag{11}$$

On the other hand, as stated in [35] the Lattice Boltzmann method converges towards the Navier–Stokes equation only if the dimensionless viscosity is related to the dimensionless relaxation time by the following expression:

$$\tau = \frac{\nu_d}{c_s^2} + \frac{1}{2}. \tag{12}$$

Here $c_s^2 = 1/3$ is the speed of sound in the lattice system [35].

The choice of time step has a strong influence on the stability and accuracy of the method. For the Reynolds numbers considered in the present analysis ($\mathrm{Re} < 1$), to obtain the solution with low level of error it is suggested [36] to choose a time step so that $0.5 < \tau < < 1.5$. The optimum was found to be around 0.9. For other values the solutions converges towards wrong solutions, or do not converge at all. In the present analysis τ is taken equal to 0.9.

To calculate the Reynolds Number we have used the physical length of the input microstructure as reference length, $l_{ref,p}$. Alternatively, we could have chosen the corresponding primary arm spacing. The reference time, $t_{ref,p}$, was taken from the relation $t_{ref,p} = l_{ref,p}/u_{ref,p}$, whereby the reference velocity was obtained with the equation for dynamic pressure:

$$u_{ref,p} = \sqrt{2\frac{\nabla_p p_p}{\rho_p}}. \tag{13}$$

To consider the pressure gradients in the LB simulations, a constant body force acting on each of the liquid lattice elements was introduced. A non-slip boundary condition is imposed at the solid/liquid interfaces by implementing a bounce-back rule that reverses the momentum of particles approaching the solid wall [30]. Periodic boundary conditions are maintained at the inlets and outlets of the domain.

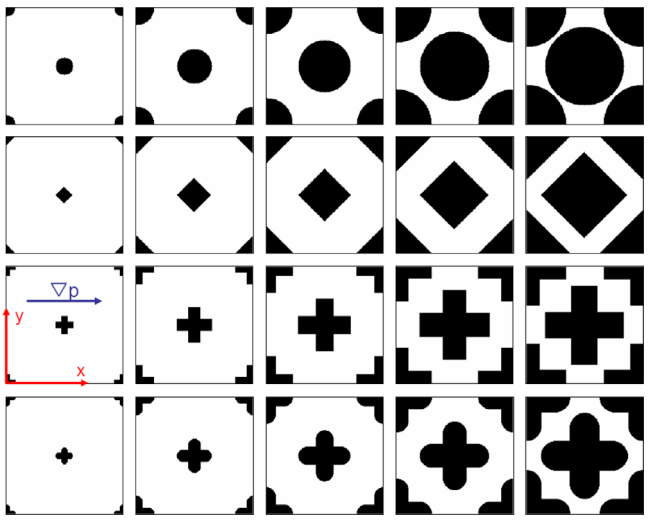

Fig. 2. Areas of circles, cubes, crosses and curves bounded crosses representing different solid fractions. The orientation of the coordinate system as well as the direction of the applied pressure gradient is also shown.

3. Input microstructures

3.1. Artificial microstructure

For the starting point of our investigation we have used predefined 2D bcc arrays of artificial solid objects as input microstructures for the LB flow simulations. Examples are shown in Fig. 2. The flow through these arrays was initiated by applying a pressure gradient of 10^{-3} Pa/mm in x-direction. Periodic boundary conditions in both directions were applied, as well as the halfway bounce back rule for the solid/liquid interface. The simulation domains were discretized with 201×201 lattice cells, which turned out to be sufficient to obtain cell size independent results. Different solid fractions were obtained by increasing the size of the objects. Obviously, the flow channels between the objects decrease with increase object size, which finally leads to complete blocking at a certain structure-dependent object size. The permeability of the predefined artificial microstructure was evaluated based on Darcy´s law as given in Eq. (1).

3.2. Phase field dendrites

In order to get a more realistic input microstructure, phase field (PF) calculations of dendritic solidification were performed. The simulated dendrite shown in Fig. 3 was obtained using the quantitative phase field model by Karma [37] for dilute binary alloys. The parameters were set to correspond to the isothermal solidification of Fe–C at temperature $T = 1780$ K, with partition coefficient $k = 0.18$ and initial melt concentration $c_0 = 0.0097$. Although the flow may generally interact with the formation of the dendritic morphology we have neglected any interaction of the flow with the growing dendritic morphology and considered the dendrite as given solid obstacle to the flow. As for the predefined artificial microstructures, we have initiated the flow by applying a constant pressure gradient of 10^{-3} Pa/mm perpendicular to the

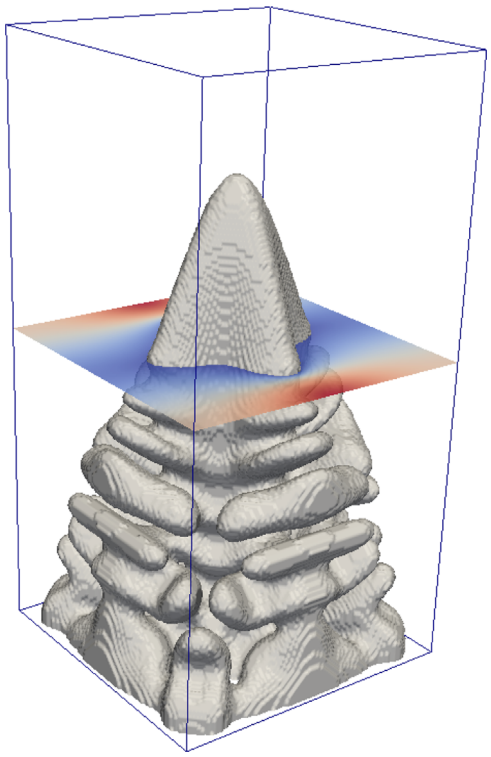

Fig. 3. Example of a dendrite obtained by phase field calculations. The vertical walls of the box represent the non-flux boundaries used for Phase Field calculation. The colored plan gives an example of the velocity-norm within this plan. (For interpretation of the references to color in this figure caption, the reader is referred to the web version of this paper.)

dendrite axis. Periodic boundary conditions were applied for all the walls except at the bottom and the top of the domain where a non-slip condition was used. The calculation domain shown in Fig. 3 had a height of 200 μm and a width of 100 μm × 100 μm. For the LB calculation it was discretized into $256 \times 128 \times 128$ lattice cells.

The velocity field was calculated in 3D for the entire domain. Based on this velocity field the permeability perpendicular to the dendritic structure was estimated. We have analyzed the flow for each plane perpendicular to the dendrite axis considering only flow components within the corresponding plane. Due to the presence of non-slipping walls the corresponding permeability values were calculated with the help of the Darcy–Brinkman equation:

$$\nabla p = -\frac{\mu_l}{K}\vec{v}_s + \mu_l \nabla^2 \vec{v}_s, \tag{14}$$

where $\vec{v}_s = g_l \vec{v}$ is the superficial velocity.

The flow parallel to the dendrite axis was also considered. For this case, the dendrite was separated into ten parts of uniform length. To allow the use of periodic boundary conditions every part was mirrored to generate a symmetric shape. In this case the permeability is extracted by using the Darcy law, Eq. (1).

3.3. Computed-tomography of an AlCu alloy

A typical dendritic microstructure as input for a LB flow simulations was captured with computed tomography (CT). Since this analysis method needs sufficient density differences to resolve different phases, a binary Al–18 wt%Cu alloy was investigated. This alloy consists of two main phases; the primary aluminum dendrites and the interdendritic eutectic. While the Al-dendrites are impoverished in Cu, the eutectic is enriched in Cu. This causes different densities which can be used in the CT to distinguish both phases. The eutectic areas were detected and numerically removed to allow the presence of void regions. The regions are believed to have been liquid at a certain stage of the solidification.

To prepare the data sample for the LB simulations, the intensity values captured with CT and representing the dendritic phase were set to 0, while those values which represent the eutectic phase were set to 1. Thus, a three-dimensional array containing values of 0 and 1 was written to a simple *.*txt*-file which was then used with the C++ library *Palabos*.

The applied periodic boundary condition in flow direction enables the flow which leaves the simulation domain through a certain boundary face "1" to enter the domain again at the opposite boundary face "2". Hence, the developing flow pattern is uninfluenced by non-linear effects which may occur if conventional inlet boundary conditions are used. However, applying the periodic condition requires pairs of boundary faces having solid and liquid lattice cells at the same position. To ensure this, the simulation domain was mirrored in the main flow direction. For all other outer boundaries, a no-slip condition was applied. Therefore this represents a channel of square cross-section filled with dendrites similar to configurations of experimental permeability investigations [38]. The array finally used for the simulations had an entire size of $400 \times 200 \times 200$ voxels which corresponds to dimensions of $960 \times 480 \times 480$ μm. More details about the CT reconstruction process can be found in [39].

As before, a pressure gradient of 10^{-3} Pa/mm was applied along the main flow direction. This comparatively low pressure gradient was chosen to achieve laminar flow through the structure. Based on the calculated flow field, the permeability of the structure was evaluated based on Darcy's law, Eq. (1).

4. Results and discussion

4.1. Artificial microstructure

Permeability data obtained from LB flow simulations through the predefined artificial microstructures are shown in Fig. 4. Our results fit well with the analytical solutions published in [22, 23] for solid fractions close to zero. The precise shape of the obstacles and their arrangement (triangular or bcc arrays) is not of significant importance. This changes if the size of the obstacles

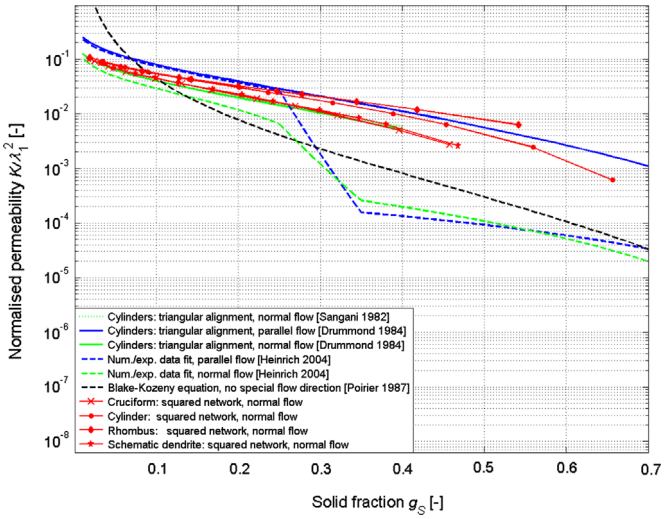

Fig. 4. Permeability of the artificial microstructures compared to different results from literature. (For interpretation of the references to color in this figure caption, the reader is referred to the web version of this paper.)

increases. Generally, we predict a deviation from the analytical solutions for increasing solid volume fractions. As stated in [22, 23] the analytical solutions are strictly valid only for very small solid volume fractions. In our case, squares and circles give similar permeability values whereas cruciforms and round-shaped cruciforms result in a higher flow resistance and thus in a lower permeability. It can be noticed that the predefined artificial microstructures only allow flow through up to a certain solid volume fraction, which can correspond to the maximum volume fraction packing limit, each curves end at the corresponding limit. In Fig. 4, the influence of the geometrical shape on the calculated permeability is clearly visible, since at $g_s \sim 0.5$ the difference in permeability reaches about one order of magnitude.

4.2. Phase field dendrites

The simulated dendrite was obtained using the quantitative phase field model by Karma [37] for dilute binary alloys. The parameters were set to correspond to the isothermal solidification of Fe–C at temperature $T=1780$ K, with partition coefficient $k=0.18$ and initial melt concentration $c_0=0.0097$. The evaluation of the flow field around the phase field dendrite shown in Fig. 3 leads to the permeability data shown in Fig. 5. For very low solid volume fraction (that's for the dendrite tip region) the results are similar to the analytical expression from [22, 23] both for flow normal and parallel to the dendrite axis. However, deviations occur when side arms start to form. For the phase field dendrites evaluated in this work, this happens at $g_s \sim 0.25$. Above this limit we found a great spread of permeability data especially for g_s between 0.25 and 0.65 especially for flow normal to the axis. In this region the secondary arms of the dendrite are dominant, and due to their inhomogeneous geometries large changes of the permeability are predicted even for almost constant solid volume fraction g_s. In addition to this effect, the solid volume fraction also varies strongly along the dendrite axis. For example, in the first 25 planes taken from lower part of the phase field dendrite the solid fraction g_s ranges from 0.86 to 0.39, which is shown in Fig. 6.

Note that the exact permeability data depend strongly on the position and on the shape of the side arm formation. In some cases also tertiary side arms may occur, which will influence the local flow resistance, and thus the permeability. The permeability jump reported in [21] can also be found in our results, namely right at the position where the secondary arms start to grow. The wide spread of permeability values at almost the same solid volume fraction shows a strong correlation between the dendritic geometry and the resulting permeability. Structures with the same solid volume fraction (Fig. 6) generate a resistance to the flow that can vary by two order of magnitude.

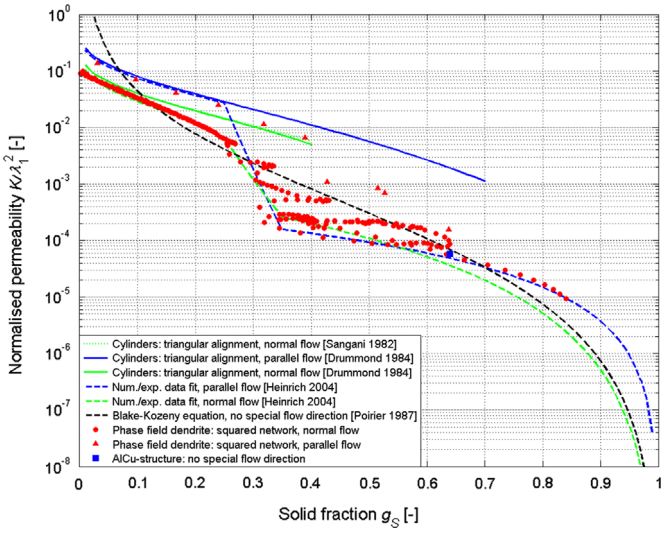

Fig. 5. Permeability values estimated by LB flow simulations normal and parallel to a phase field dendrite shown in Fig. 3 compared with the literature data. The black arrow points to the single result obtained for the LB flow simulation through the AlCu tomogram. (For interpretation of the references to color in this figure caption, the reader is referred to the web version of this paper.)

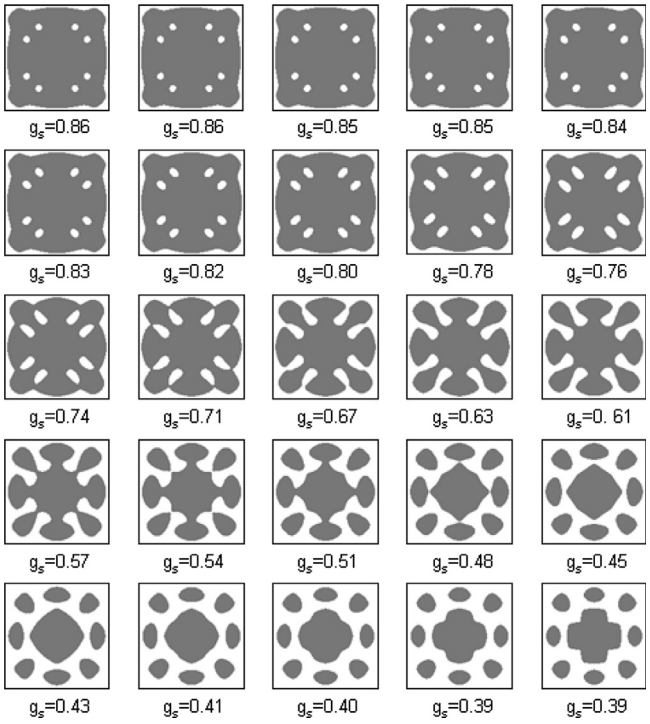

Fig. 6. Cross sections perpendicular to the axis of the phase field dendrite (Fig. 3) with different solid fractions.

For a solid volume fraction larger than around 0.6, the permeability values estimated from the flow normal to the dendrite steam become unique. This might due to the fact that for the present dendrite, such high solid volume fractions occur only once. However, the possibility of forming generally different flow patterns at high solid volume fraction is limited compared to possibility which exist at lower solid fraction. This might be a hind of the nature of the permeability data spread found in literature. It is interesting to notice that for the largest solid fractions, the calculated permeabilities are in good agreement with the prediction of the anisotropic Black-Kozeny law.

For parallel flow the results are similar to the one provided by Drummond's analytical approximation, but only until the formation of side arms. With developed side arms the flow resistance increases and therefore the permeability decreased compared to the cylinders considered by Drummond [23].

4.3. Computed tomography of an AlCu alloy

Streamlines of the flow passing through the eutectic structure are shown in Fig. 7. With only one structure being investigated so far, results could not be plotted as a function of solid volume fraction yet. The average primary arm spacing was estimated to be $\sim 220\,\mu$m, and the solid fraction of the sample is $g_s=0.64$. The permeability computed from the result of the flow field through the interdendritic spacing was found to be equal to $K=2.8 \times 10^{-12}$ m^2. This result is reported in Fig. 5, its value for

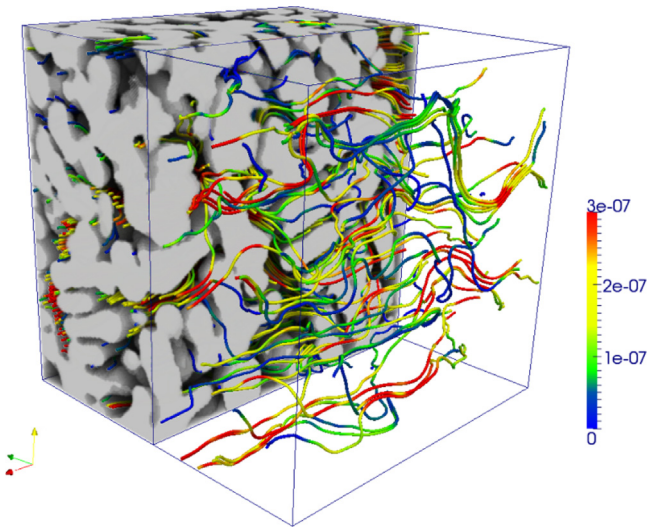

Fig. 7. Streamlines passing through the structure of $200 \times 200 \times 200$ voxels for simulation with an applied pressure gradient of 10^{-1} Pa/mm. To visualize the streamlines one half of the structure is hidden. (For interpretation of the references to color in this figure caption, the reader is referred to the web version of this paper.)

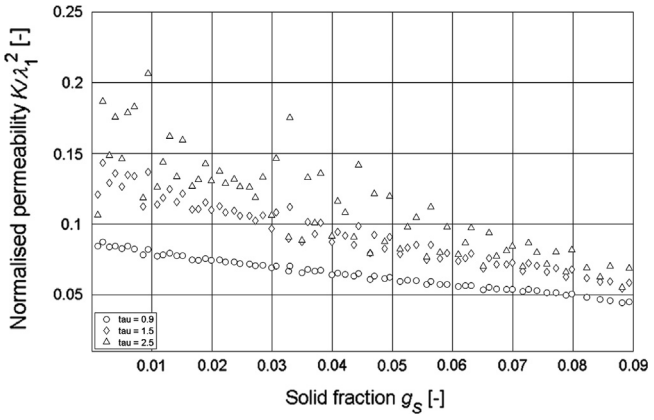

Fig. 8. Permeability for different relaxation coefficients τ , results zoomed near the dendrite tip.

the corresponding solid fraction is in excellent agreement with the previous results obtained by using the phase field dendrite.

5. Numerical accuracy

All previous results were calculated for the dendrite shown in Fig. 3 with $\tau=0.9$ and reported after having reached a residual of variable change smaller than 10^{-7}. Good agreement was found with theoretical and *Finite Volume* results for $f_s < 0.25$ (Fig. 5). In order to show the sensitivity of the calculated permeability on the relaxation coefficient τ, calculations were performed for $\tau=0.3$, 1.5, 2.5, and 5. Since the grid size is fixed, changing τ means changing the time step. As predicted in [36] no convergence was achieved for $\tau=0.3$ and 5.

For $\tau=1.5$ and 2.5 the results did converge but towards different solutions from the one obtained with $\tau=0.9$ (see Fig. 8) Permeabilities are about 50% higher for $\tau=1.5$, and 100% higher for $\tau=2.5$. However, higher level of scattering is also found for $\tau=2.5$, which is a sign that a limit in computation stability is approached. Special care must be given to the free parameters of the Lattice-Boltzmann simulation if accuracy is targeted.

6. Conclusions

Reliable permeability data of semi-solid dendritic networks are essential for predicting macrosegregation in castings. The three methods of getting an input microstructure for flow simulations showed that analytical/numerical approximations for predefined artificial microstructures may give good data for low solid volume fraction. However, for microstructures which are mainly governed by the presence of any type of side arms, permeability data varies even for similar solid volume fractions. This seems to be an intrinsic fact which represents the possibility of having different flow resistances at the same solid volume fraction or of having the some flow resistance at different solid volume fractions, both caused by a different local morphology. At large solid volume fraction, the morphology resembles a volume of packed spheres, in which the liquid flows through multiples channels. Thus the diversity of morphology disappears, leading to a single value for the permeability.

Acknowledgment

This work is financially supported by the Austrian Christian-Doppler Research Society, the Material Center Leoben, voestalpine Stahl Linz, Siemens-VAI Metal Technologies, and voestalpine Stahl Donawitz.

References

[1] Apelian D, Flemings MC, Mehrabian R. Metall Trans 1974;5:2533–7.
[2] Hubbert MK. The theory of ground-water motion and related papers. New York, NY: Hafner Publishing Company; 1969; 303–11.
[3] Poirier DR. Metall Trans B 1987;18:245–55.
[4] Ganesan S, Poirier DR. Metall Trans B 1990;21:173–81.
[5] Ganesan S, Chan CL, Poirier DR. Mater Sci Eng A 1992;151:97–105.
[6] Fabietti L, Sekhar. J. Metall Mater Trans A 1992;23:3361–8.
[7] Poirier DP, Ganesan S. Mater Sci Eng A 1992;157:113–23.
[8] Bhat MS, Poirier DR, Heinrich JC, Nagelhou D. Scr Metall Mater 1994;31:339–44.
[9] Wang CY, Ahuja S, Beckermann C, de Groh III HC. Metall Trans B 1995;26:111–9.
[10] Bhat MS, Poirier DR, Heinrich JC. Metall Mater Trans B 1995;26 (1049-1056 and 1091–1092).
[11] Goyeau B, Benihaddadene T, Gobin D, Quintard M. Metall Trans B 1999;30:613–22.
[12] Poirier DR, Heinrich JC, Erdmann RG, Bhat MS. In: Abbaschian R, Brody H, Mortensen A, editors. Proceedings of the Merton C. Flemings symposium on solidification and materials processing. Warrendale, PA: TMS; 2001. p. 287–96.
[13] Brown SGR, Spittle JA, Jarvis DJ, Walden-Bevan R. Acta Mater 2002;50: 1559–1569.
[14] Mirbagheri SMH, Chirazi A. Mater Sci Eng A 2006;427:51–9.
[15] Fuloria D, Lee PD, Bernard D. Mater Sci Eng A 2008;494:3–9.
[16] Khajeh E, Mirbagheri SMH, Davami P. Mater Sci Eng A 2008;475:355–64.
[17] Poirier DR, Ocansey P. Mater Sci Eng A 1993;171:231–40.
[18] Bhat M.S. Numerical calculation of permeability in dendritic alloys (PhD thesis). University of Arizona; 1995.
[19] Goyeau B, Benihaddadene T, Gobin D, Quintard M. Transp Porous Media 1997;28:19–50.
[20] Erdmann RG, Image-based numerical simulation of Stokes flow in porous media (PhD thesis). University of Arizona; 2006.
[21] Heinrich JC, Poirier DR. C R Mec 2004;332:429–45.
[22] Sangani AS, Acrivos A. Int J Multiphase Flow 1982;8:193–206.
[23] Drummond JE, Tahir MI. Int J Multiphase Flow 1984;10:515–40.
[24] Schneider MC, Gu JP, Beckermann C, Boettinger WJ, Kattner UR. Metall Mater Trans A 1997;28:1517–31.
[25] Murakami K, Shiraishi A, Okamoto T. Acta Metall 1983;31:1417–24.
[26] Murakami K, Shiraishi A, Okamoto T. Acta Metall 1984;32:1423–8.
[27] Nandapurkar P, Poirier DR, Heinrich JC. Numer Heat Transf 1991;19A: 297–311.
[28] ⟨http://www.lbmethod.org/palabos/documentation.userguide/index.html⟩.
[29] Qian YH, D'Humieres D, Lallemand P. Europhys Lett 1992;17:479–84.
[30] Ziegler DP. J Stat Phys 1993;71:1171–7.
[31] Chen S, Doolen GD. Annu Rev Fluid Mech 1998;30:329–64.
[32] Succi S. The Lattice Boltzmann equation for fluid dynamics and beyond. Oxford: Clarendon Press; 2001.
[33] Feng YT, Han K, Owen DRJ. Int J Numer Methods Eng 2007;72:1111–34.
[34] Bhatnagar PL, Gross EP, Krook M. Phys Rev 1954;94:511–25.

[35] He X, Luo L-S. J Stat Phys 1997;88:927–44.
[36] Holdych DJ, Noble DR, Georgiadis JG, Buckius RO. J Comp Phys 2004;193:595–601.
[37] Karma A. Phys Rev Lett 2001;87:115701–5.
[38] Khajeh E, Maijer DM. Acta Mater 2010;58:6334–44.
[39] Domitner J., Hölzl C., Kharicha A., Wu M., Ludwig A., Köhler M., et al. In: Third International conference on advances in solidification processes (ICASP-3), IOP conference series: Materials Science Engineering, vol. 27; 2011. p. 012016.